

See discussions, stats, and author profiles for this publication at: <https://www.researchgate.net/publication/327309260>

pH-sensitive and biodegradable charge-transfer nanocomplex for second near-infrared photoacoustic tumor imaging

Article in *Nano Research* · August 2018

DOI: 10.1007/s12274-018-2175-9

CITATIONS

0

READS

46

14 authors, including:



Zhimin Wang

Nanyang Technological University

17 PUBLICATIONS 109 CITATIONS

[SEE PROFILE](#)



Paul Kumar Upputuri

Nanyang Technological University

68 PUBLICATIONS 837 CITATIONS

[SEE PROFILE](#)



Xu Zhen

Nanyang Technological University

59 PUBLICATIONS 858 CITATIONS

[SEE PROFILE](#)

Some of the authors of this publication are also working on these related projects:



Triphenylphosphonium Derivatives as Anti-tumour Prodrugs [View project](#)



Biomedical imaging using microfluidics- based double emulsions as contrast agents [View project](#)

pH-sensitive and biodegradable charge-transfer nanocomplex for second near-infrared photoacoustic tumor imaging

Zhimin Wang¹, Paul Kumar Upputuri², Xu Zhen², Ruochong Zhang³, Yuyan Jiang², Xiangzhao Ai¹, Zhijun Zhang¹, Ming Hu¹, Zhenyu Meng¹, Yunpeng Lu¹, Yuanjing Zheng³, Kanyi Pu², Manojit Pramanik² (✉), and Bengang Xing¹ (✉)

¹ Division of Chemistry and Biological Chemistry, School of Physical & Mathematical Sciences, Nanyang Technological University, Singapore 637371, Singapore

² School of Chemical and Biomedical Engineering, Nanyang Technological University, 70 Nanyang Drive, Singapore 637459, Singapore

³ School of Electrical and Electronic Engineering, Nanyang Technological University, 50 Nanyang Avenue, Singapore 639798, Singapore

© Tsinghua University Press and Springer-Verlag GmbH Germany, part of Springer Nature 2018

Received: 12 June 2018 / Revised: 12 August 2018 / Accepted: 13 August 2018

ABSTRACT

The emerging technique of photoacoustic imaging, especially in the near infra-red (NIR) window, permits high resolution, deep-penetration, clinically reliable sensing. However, few contrast agents are available that can specifically respond to intricate biological environments, and which are biodegradable and biocompatible. Herein, we introduce a new class of pH-sensitive organic photoacoustic contrast agent that operates in the second NIR window (NIR-II, 960–1,700 nm), which is derived from the self-assembled charge-transfer nanocomplex (CTN) by 3,3',5,5'-tetramethylbenzidine (TMB) and its dication structure (TMB⁺⁺). The unique NIR-II-responsive CTN can specifically respond to pH change in the physiological range and allows noninvasive and sensitive visualization of the tumor acidic microenvironment (e.g. at pH 5) in mice with higher signal-to-noise ratio. The CTN is biodegradable under physiological conditions (e.g. pH 7.4), which alleviates the biosafety concern of nanoparticle accumulation *in vivo*. These results clearly show the potential of the TMB/TMB⁺⁺-based CTN as a promising pH-activated and biodegradable molecular probe for specific tumor photoacoustic imaging in the NIR-II region.

KEYWORDS

charge-transfer nanocomplex, second near-infrared window, photoacoustic imaging, pH-sensitive, biodegradable, tumor acidic microenvironment

1 Introduction

Photoacoustic imaging (PAI) is an emerging hybrid biomedical analysis technique that provides reliable sensing at penetration depths and spatial resolutions that are close to practical requirements. These attributes may overcome the limitations of conventional optical imaging, such as low penetration and light diffusion, and ultrasonic imaging (e.g. low contrast). PAI thus is potentially valuable for clinical translation [1–6].

Despite this potential, conventional PAI for numerous biomedical applications based on intrinsic or extrinsic contrasts are still flawed due to the overwhelming light scattering of biological tissues and serious nonspecific PA signal readout [1, 7]. Remarkable efforts to technically improve the quality of PAI have included the engineering of more sensitive photoacoustic setups and the development of more efficient contrast agents [8–10]. The development of the commercially available Q-switched Nd:YAG pulse-laser (1,064 nm) and new second near infra-red (NIR) window (NIR-II, 960–1,700 nm) light-absorbing PA contrast materials, including silver nanoplates, copper sulfide nanoparticles, phosphorus phthalocyanine, and semiconducting polymer nanoplateforms, allow photoacoustic sensing in the NIR-II window. NIR-II PA imaging has received worthy attention in deep tissue, brain vasculature, and tumor detection due to its centimeter-deep penetration and higher signal-to-noise ratio (SNR) [11–18]. However, these NIR-II PA contrast agents still face challenges for *in vivo* applications, since the endogenous NIR-II

absorption and non-targeted contrast extravasation dramatically affect the imaging sensitivity and specificity. In addition, the biological incompatibility and long-term accumulation of these PA contrast agents have raised concerns for their biosafety in practice [9, 11]. Some NIR-II contrast agents have been designed for targeted PA imaging by conjugation with targeting moieties, such as antibodies, intelligent and environment-responsive NIR-II PA sensing has not yet been fully realized [12, 19–21]. Therefore, the development of sensitive and biodegradable NIR-II PA imaging probes that can specifically respond to external stimulation for more reliable molecular sensing of various biological and pathological implications, and more importantly, can potentially realize successful clinical translations are highly desired [22, 23].

Charge-transfer complex (CTC) materials are assemblies of charge-donating (D) and charge-accepting (A) molecules that have been intensely studied for several decades due to their wide range of properties, such as the anisotropic conductivity, photoconductivity, paramagnetism, ferroelectricity, and ambipolar transport [24–30]. Extensive investigations of intramolecular CT (ICT) have shown that the excitation energy of the transitional state can contribute to the formation of typical CT bands in the visible and NIR regions in the electromagnetic spectrum, which results in an intense light harvesting. These CTC materials are expected to have multi-field applications in solar cells, ferromagnets, superconductors, sensors, and devices [31–33]. In particular, the colorimetric assay based on the formation of charge-transfer nanocomplex (CTN) by 3,3',5,5'-

Address correspondence to Bengang Xing, Bengang@ntu.edu.sg; Manojit Pramanik, manojit@ntu.edu.sg

tetramethylbenzidine (TMB) and cationic TMB (diiminium cation, TMB⁺⁺) has been applied for detection of free radicals, blood testing, and the enzyme-linked immunosorbent assay (ELISA) in preclinical research and clinical practice [34–36]. Preliminary studies also disclosed that the TMB⁺⁺ oxidation product can accept the electron (or charge) of TMB and produce the CTN, which is responsible for the blue colored CT bands with maximum absorbance at 370 and 652 nm. Further oxidation of the cationic TMB⁺⁺ or moderate changes in pH yield a yellow diimine product (maximum absorbance at 450 nm), resulting in the degradation of CTN (Fig. 1(a)) [34, 37, 38].

Interestingly, we recently observed that this CTN shows one more broadband NIR absorption peak ranging from 750 to 1,200 nm on the optical spectrum (Fig. 1(b)) [38]. Such a strong absorption band could be greatly enhanced in the acidic environment (pH 5) compared to the neutral or slight basic condition (pH \geq 7), which provides the feasibility to enable CTN as a promising pH-sensitive NIR-II absorber for biological applications. The tumor microenvironment is acidic, probably due to the glycolytic metabolism and deficient blood perfusion. This microenvironment is significant for tumor cell proliferation, metastasis, and chemoresistance [39–41]. Accordingly, a low tumor pH has been widely regarded as an effective strategy for tumor diagnostic and therapeutic purposes [42–44]. In terms of the unique pH-responsive feature of CTN, in this study, the broadband NIR-absorbing and environment-sensitive CTN could be a promising pH-activatable PA probe for specific and sensitive sensing of tumor acidic microenvironment. Considering the biomedical applicability of this TMB/TMB⁺⁺ based CTN, the potential cytotoxicity and clearance was evaluated in combination with biosafety of TMB [45–47].

2 Experimental

2.1 Preparation, diameter optimization, and characterization of CTN

TMB and silver nitrate were purchased from Sigma-Aldrich. Unless otherwise stated, all commercial available reagents for synthesis and assays were used without further purification. CTN nanofibers were prepared and characterized according to a previously reported method with slight modifications [48]. Typically, 1 mL of AgNO₃ aqueous solutions with different concentrations (1–20 mM) were added to 2 mL of TMB (10 mM) ethanol solution with vigorous stirring at room temperature. The color of the reaction mixture started to change from green to dark purple after the reaction had proceeded for 2 h. The uppermost purple CTN nanofibers were collected by centrifugation and then washed twice with deionized (DI) water for the subsequent experiments. The gray, precipitated Ag nanoplates at the bottom were removed. Ultraviolet–visible (UV–Vis)–NIR absorption spectra were measured using a Lambda 950 spectrometer (Perkin Elmer). CTN morphology was investigated using a JEOL JSM-6700F field emission scanning electron microscope. A Bruker D8 X-ray diffraction (XRD) system, Perkin-Elmer model PHI 5600 X-ray photoelectron spectroscopy (XPS) system, and a Bruker Vertex 80v vacuum Fourier-transform infra-red (FTIR) spectrometer were used for structure analyses.

2.2 Cell culture and cytotoxicity test

NIH/3T3 mouse embryo fibroblast cells and RAW 264.7 murine macrophage cells were purchased from American Type Culture Collection. The cells were cultured in Dulbecco's modified Eagle's medium (DMEM) with 10% calf bovine serum (CBS) containing penicillin (100 IU/mL) and streptomycin (100 μ g/mL) and maintained in an atmosphere containing 5% CO₂ and 95% humidified air at 37 °C. For the cytotoxicity test of CTN, both cell lines were

independently seeded in 96-well plates (100 μ L containing approximately 8,000 cells/well) and incubated for 24 h. Different concentrations of CTN were added to the cell culture medium, then the cells were incubated for 24 h. The medium was removed and washed with phosphate buffered saline (PBS). Fresh cell culture medium containing TOX8 was then added to wells and plates were incubated for 3 h. The fluorescence at 590 nm was measured using a Tecan Infinite M200 microplate reader at an excitation wavelength of 560 nm. Cell viability was expressed as the ratio of the fluorescence of cells incubated with CTN to that of control cells.

2.3 *In vitro* PA signal test of CTN

The laser source used is from an optical parametric oscillator tunable (700–1,200 nm) wavelength and fiber coupling. The output light from the fiber was collimated and focused by a condenser lens on the sample with an approximate spot size diameter of 500 μ m. A beam splitter and photodiode were utilized to monitor the laser intensity variation. During the experiment, the maximum permissible exposure was well within the ANSI standard. An ultrasound transducer (V303SU, Olympus) with 2 MHz central frequency was placed close to the sample to detect the PA resonance signals. The transducer was immersed in a water tank for optimum optical and acoustic coupling. The PA resonance signals were first amplified by a low-noise amplifier (5662, Olympus) with a 54 dB gain, and then recorded using an oscilloscope (LeCroy) with 500 MS/s sampling rate. Peak-to-peak voltage of the PA signals were normalized with the laser energy at each wavelength and plotted against the wavelength to generate the PA spectrum of CTN.

For the concentration-dependent 1,064 nm PA testing of CTN, a Q-switched Nd:YAG pump laser was used as the laser source of PA instrumentation. CTN solutions or fresh mouse blood were placed inside a low-density polyethylene (LDPE) tube with an inner diameter of 0.59 mm and outer diameter of 0.78 mm. An LDPE tube containing samples and a single-element ultrasound transducer (UST, V323-SU/2.25 MHz, 13 mm active area, and 70% nominal bandwidth; Panametrics) were both immersed in water for coupling of PA signals to the UST. The LDPE tube was irradiated with laser pulses at a wavelength of 1,064 nm. PA signals were collected by the UST, amplified with a gain of 50 dB, and subsequently band pass filtered (1–10 MHz) by a pulse/receiver unit (5072PR, Olympus-NDT). Finally, the output signals from the pulser/receiver unit were digitized with a data acquisition card (DAQ, GaGe, Compuscope 4227) operated at 25 MHz and the acquired signals were stored in the computer. PA signals of with different concentrations of CTN at 1,064 nm were measured and plotted.

2.4 Deep tissue NIR-II PAI of CTN

CTN spots of three different concentrations were embedded in an agar gel phantom (0.1, 0.5, and 1 mg/mL). Chicken breast tissues were stacked layer-by-layer above the agar gel phantom to obtain various imaging depths. A home-made PA tomography system was used for deep tissue and tumor imaging. The system uses a high energy Q-switched 1,064 nm Nd:YAG laser (Continuum, Surelite Ex) as a PA excitation source. The laser can deliver 5 ns pulses at 10 Hz repetition rate. The near-infrared 1,064 nm beam was delivered to the ultrasound scanner through right angle prisms. The narrow laser beam was expanded and homogenized using an optical diffuser. The UST was immersed in water for coupling the PA signal from the sample to the transducer. The PA signals generated by the tumor were received by a single-element transducer (V323-SU/2.25 MHz, Olympus NDT). The UST had a 13 mm active area and 70% nominal bandwidth. The UST was continuously rotated in a circular geometry by a stepper motor to acquire PA signals from all angles of the tissue and tumor. The collected signals were subsequently amplified, band-pass filtered (1–10 MHz) by an ultrasound amplifier

and filter unit (A/F, 5072, Olympus NDT) and then digitized. The signals were recorded using a PC with a 25 Ms/s data acquisition (DAQ) card from GaGe (Compuscope 4227). Finally, the acquired PA signals were used to reconstruct the tumor image using a delay-and-sum back projection algorithm.

2.5 *In vivo* NIR-II PAI of tumor

In vivo PAI of tumor-bearing female NCr nude mice was acquired by the homemade 1,064 nm PAI system mentioned above. Animal experiments were performed in accordance with the approved guidelines and regulations, and were approved by the institutional Animal Care and Use committee of Nanyang Technological University, Singapore (Animal Protocol Number ARF-SBS/NIE-A0263). 4T1 xenograft tumor cells (2×10^6) suspended in 0.2 mL of DMEM containing 10% fetal bovine serum (FBS) and 1% antibiotics were subcutaneously injected into one side of the backs of the mice. After two weeks, the tumor-bearing mice were used for 1,064 nm PA imaging. A layer of ultrasonic coupling gel was applied on each mouse's skin at the tumor area. The mouse was subsequently anesthetized and placed into the PA setup with the tumor protruding above to the water tank through a hole that was sealed by transparent polyethylene film. The tumor-bearing mouse and the control mouse without tumor were monitored and imaged before and after intratumoral or subcutaneous injection of CTN (1 mg/mL, 200 μ L per mouse, $n = 3$) using the 1,064 nm laser with a power intensity of 5.5 mJ/cm². At different post injection times, PA images were acquired and reconstructed for the tumor and the normal tissue.

3 Results and discussion

3.1 Preparation and characterization of CTN

The CTN material used was prepared as shown in Fig. 1(a) [48]. The diameter optimization was achieved through alteration of the

relative concentration of the substrates (TMB and AgNO₃), wherein the intermolecular charge-transfer degree of the π -conjugated push-pull system was controllable. As shown in Fig. 1(c) and Fig. S1 in the Electronic Supplementary Material (ESM), the diameters of the prepared CTN varied from 418.4 ± 15.4 to 79.6 ± 2.2 nm and the optimal sized CTN (< 100 nm) was chosen as the candidate for further investigation. The XRD analysis (Fig. S2(a) in the ESM) indicated that the peaks at 10.5, 17.4, and the broad peak could be ascribed to the formation of organic CTN by the charge-transfer process between TMB and TMB⁺⁺. The XPS data presented in Fig. S2(b) show the occurrence of carbon, oxygen, and nitrogen signals. The peaks at 401.9 and 399.8 eV in the N1s high-resolution XPS spectrum (Fig. 1(d)) could be assigned to the protonated imine TMB⁺⁺ and the neutral amine TMB of CTN. Differences in the FTIR spectra (Fig. S2(c) in the ESM) between TMB and CTN could also be direct evidence for the formation of CTN containing the typical phenyl ring of TMB and C=N bond of quinonediimine, like the cation (TMB⁺⁺). To further validate the charge-transfer of CTN, we carried out computational analysis using Gaussian 09 under the HF/6-31+G(d,p) scheme [49]. The simulated molecular orbitals in Fig. 1(e) showed that the energy level of the lowest uncoupled molecular orbital of TMB⁺⁺ (-7.0341 eV) was lower than that of TMB with an energy-gap of 0.0468 eV, which demonstrated the possibility of the CT process from TMB to TMB⁺⁺. The collective results deduced the structure and charge-transfer mechanism of the prepared CTN.

3.2 *In vitro* photoacoustic performance of CTN

As shown in Fig. 2(a), the optical spectrum of the CTN aqueous solution exhibited a broadband absorption ranging from the NIR-I to NIR-II window, which can be attributed to the CT bands of TMB/TMB⁺⁺-based CTN. Most importantly, this pH-sensitive CTN was highly stable in an acidic environment (PBS, pH 5.0) for 72 h, while it was gradually degraded under normal physiological

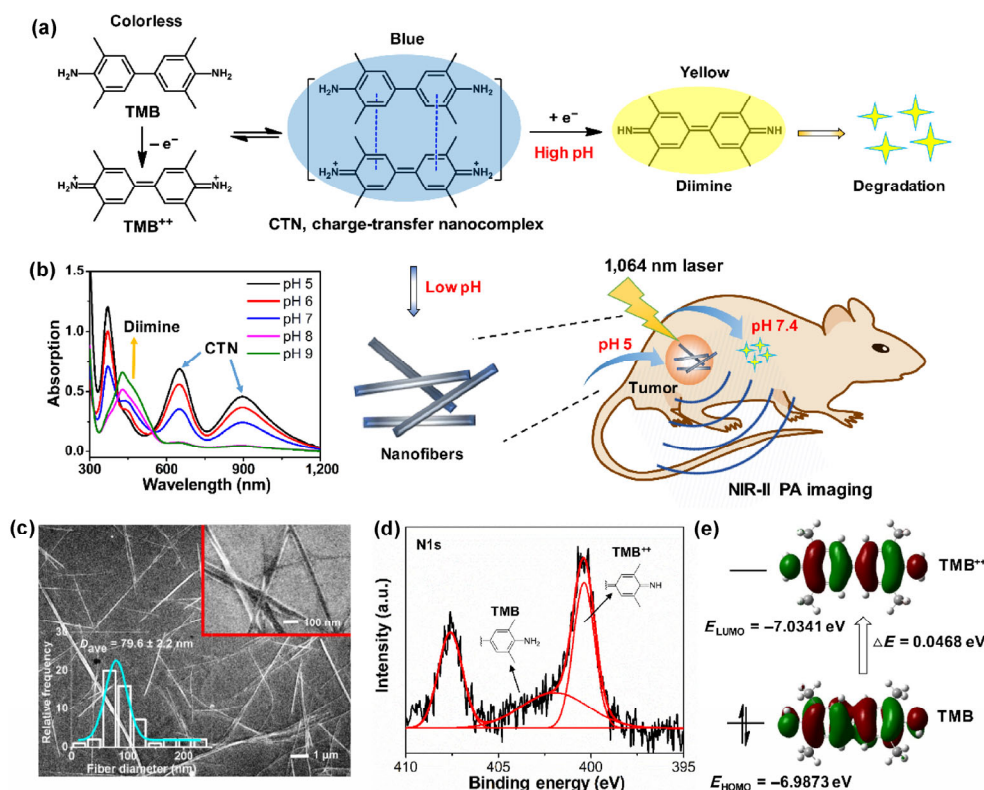


Figure 1 Preparation and characterization of CTN. (a) Schematic illustration of CTN formation, degradation, and *in vivo* NIR-II PA imaging. (b) UV-Vis-NIR absorption spectra of CTN in different pH conditions. (c) SEM images and diameter distribution of CTN. (d) High resolution XPS spectrum of CTN (N1s). (e) Frontier molecular orbitals and relative energy level of TMB and TMB⁺⁺.

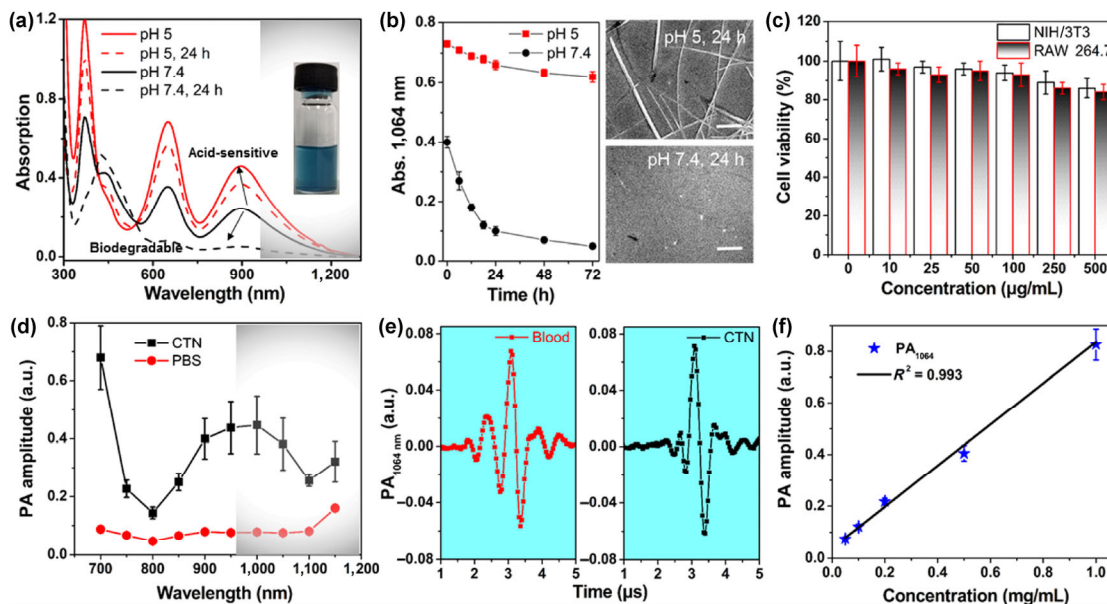


Figure 2 *In vitro* studies of CTN. (a) UV-Vis-NIR absorption spectra of CTN (0.05 mg/mL) in different PBS buffers (pH 5 and pH 7.4). (b) Sensitivity evaluation of CTN in different PBS buffers within 72 h, scale bar, 1 μm . (c) Cell viability of NIH/3T3 and RAW 264.7 cells after 24 h incubation with CTN at different concentrations. (d) Normalized PA spectra of CTN and PBS. (e) PA signal of CTN (0.1 mg/mL) and fresh mouse blood at 1,064 nm. (f) Plot of the PA amplitude at 1,064 nm as a function of CTN concentration.

conditions (pH 7.4) (Figs. 1(b) and 2(b)). Such a pH-responsive phenomenon of CTN could likely be attributed to the different charge-transfer efficiency between TMB and TMB^{++} upon their exposure to varying pH conditions [50, 51]. In addition, the potential changes of the CTN structure in different pH environments were monitored by scanning electron microscopy (SEM) after incubation with different buffers after 24 h (Fig. 2(b)). The images clearly showed that the CTN nanofibers were almost degraded in pH 7.4 PBS buffer, whereas no morphological changes were observed in the acidic condition. Therefore, the pH-sensitivity and biodegradability of such CTN could not only act as a valuable feature for a specific response to the critical parameter of pH in physiological and pathological processes (e.g. tumor acidity), but also as a property that will alleviate the health risk caused by nanoparticle enrichment *in vivo* [52, 53]. Moreover, CTN was incubated with two different cell lines, HEK293 human embryonic kidney cells and RAW 264.7 mouse macrophages for 24 h. No statistical difference in the cell viability was found with either cell type, even at concentrations up to 500 $\mu\text{g/mL}$ (Fig. 2(c)), which indicated good biosafety for potential biological applications. We further evaluated the feasibility of CTN as an NIR-II PA contrast agent. Considering the lower native

absorption from the tissue components in the NIR-II region, as a proof of concept we mainly monitored the PA signal of CTN with 1,064 nm laser excitation. The PA spectra in an aqueous solution were collected and normalized by a tunable pulse-laser illumination from 700 to 1,200 nm (Fig. 2(d)). The data suggested that CTN is suitable for NIR-II PA imaging due to the excellent photon-caustic converting efficacy [11]. In addition, to reasonably optimize the amount of CTN used for efficient PA imaging contrast at 1,064 nm, we determined through comparison with the PA signal of fresh mouse blood and found that the critical concentration of CTN was 0.1 mg/mL (Fig. 2(e)). Importantly, the linear correlation between the concentration of CTN and PA intensity at 1,064 nm was observed in Fig. 2(f) with $R^2 = 0.995$, indicating the applicability for the potential of PAI quantification. These results suggest that CTN could act as an attractive contrast candidate for NIR-II PA bioimaging and sensing purposes.

3.3 Deep tissue PAI

To validate the availability of CTN for *in vivo* application, we first tested the penetrating ability of 1,064 nm PAI with a tissue mimicking phantom made of agar gel embedded with CTN (Fig. 3(a)),

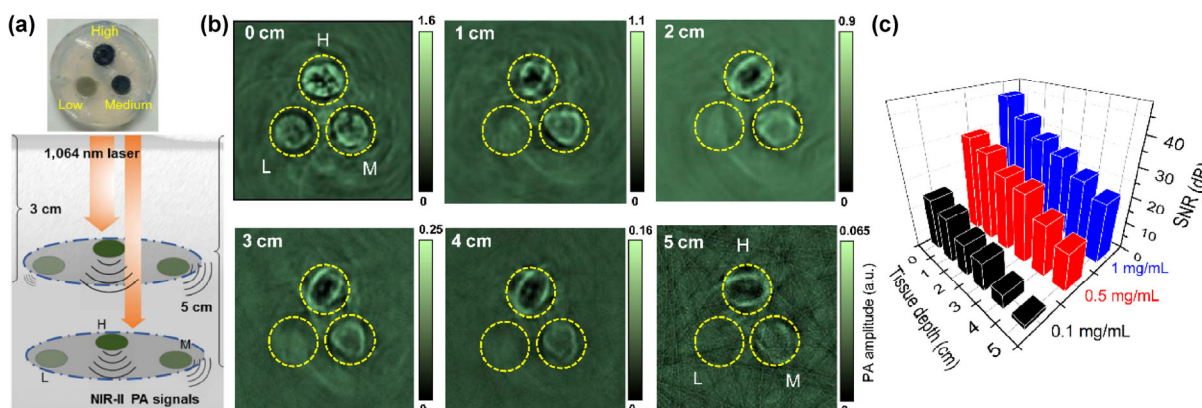


Figure 3 Deep tissue NIR-II PA imaging. (a) Agar gel phantom with different concentrations of CTN (0.1, 0.5, and 1 mg/mL) and schematic illustration for deep tissue penetration of NIR-II PAI. (b) Two-dimensional PA images at different depths (0 to 5 cm) with stacked chicken breast muscle blocks using a laser energy density of 20 mJ/cm^2 . (c) Plot of SNR with different CTN concentrations at 1,064 nm as a function of the tissue depth.

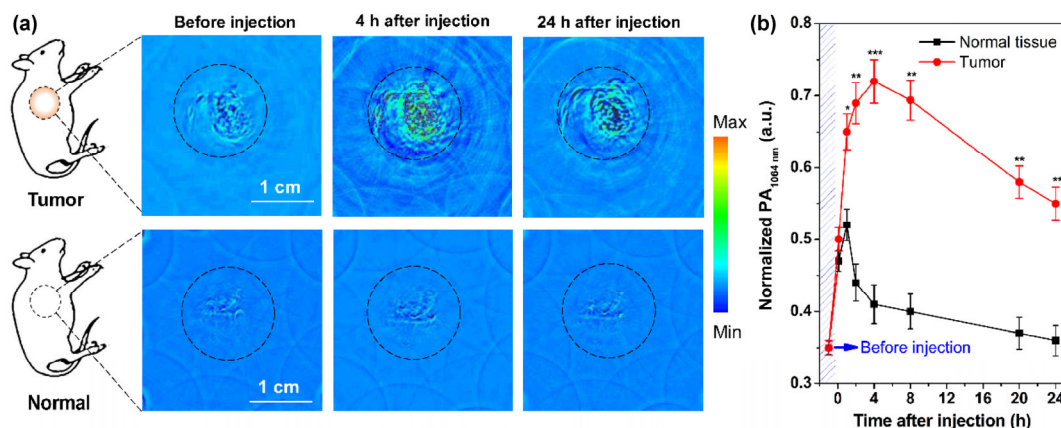


Figure 4 *In vivo* NIR-II PAI of tumor. (a) Representative PA images of the 4T1 tumor bearing mice and normal mice before and post-injection of CTN. (b) Normalized mean PA amplitudes as a function of time at 1,064 nm. Energy density was 5.5 mJ/cm². A statistically significant difference in PA amplitude (a.u.) was evident between tumor and normal tissue (**p* < 0.05, ***p* < 0.01, ****p* < 0.001, *n* = 3).

in which chicken breast muscles were arranged to achieve different thicknesses (Fig. S3 in the ESM). The PA images were obtained by increasing tissue depths from 0 to 5 cm. As shown in Fig. 3(b), all the agar gel cylinders with the three different concentrations (0.1, 0.5, and 1 mg/mL) of CTN were clearly visualized, indicating the promising PA contrast of CTN and the superior feature of NIR-II imaging. However, the signal-to-noise ratio of the reconstructed images gradually decreased with the increased depths of the chicken breast tissues (Fig. 3(c) and Fig. S4 in the ESM). It is noteworthy that the PA penetration of 0.1 mg/mL CTN was able to reach a tissue depth of approximately 3 cm, while the signal of agar gel objects with higher concentrations (CTN, 0.5 and 1 mg/mL) remained detectable even up to 5 cm tissue depth. The data indicated the advantages of NIR-II PAI for deep penetration and high-contrast in the particle bioimaging trials.

3.4 *In vivo* PAI of tumor

To further examine the imaging capability of CTN for tumor sensing *in vivo*, PA scanning of 4T1 tumor-bearing mice was conducted using the homemade PA setup under pulsed laser excitation wavelength of 1,064 nm (Fig. S5 in the ESM) [54]. Two hundred microliters of CTN (1 mg/mL) was intratumorally injected into the tumor-bearing mice. The control mice were treated with the same amount of CTN by subcutaneous injection. As shown in Fig. 4, prior to the injection of CTN, only PA signals of the background noise were observed in both tumor-bearing and control mice. The noise was derived from the tissues' absorption in NIR-II region. Five minutes after CTN injection, PA signals were obvious in the tumor area and normal tissue, with no significant difference at this stage. The PA amplitudes in the tumor became markedly enhanced over time, which was attributed to the CTN response in the acidic tumor microenvironment. In contrast, the mean PA intensity at the focused region of the control mice was gradually weakened, mainly due to the degradation of CTN under the normal physiological condition. At 4 h post-injection, an extremely significant difference (*p* < 0.001) of PA intensity was observed between tumor and normal tissue. After 24 h, there were no detectable PA signals in control mice, whereas the tumor-bearing mice still showed significant PA signals, which corresponded to the pH-sensitivity investigations of CTN *in vitro* (Fig. 2(b)). The results demonstrated the capability of CTN as a sensitive NIR-II PA probe for tumor imaging.

4 Conclusions

We successfully developed a novel, organic self-assembled, pH-sensitive, and biodegradable PA CTN probe for NIR-II PA tumor

imaging in mice. The results demonstrated the suitability of CTN for *in vivo* NIR-II PA imaging with good contrast and deep penetration up to 5 cm due to the strong CT band in the NIR-II region where the tissue background was minimal. The self-assembled CTNs were pH-responsive and the PA signal was significantly enhanced in acidic conditions compared to neutral conditions, which allows specific sensing of the tumor acidic microenvironment. More important, the biodegradable feature of CTN in a physiological condition (pH 7.4) and the preliminary cell viability evaluation indicated a negligible biosafety concern. Biosafety is particularly vital for *in vivo* imaging applications. Refinements of this CTN to improve the sensitivity or specific targeting, as well as functional diversification, will allow for better biocompatibility and utility *in vivo*. Overall, this TMB/TMB⁺⁺-based organic CTN will serve as a new class of NIR-II PA contrast agent and also as a pH-activatable probe for tumor imaging in mice. Given the many merits of CTN, we believe that such NIR-II light absorbing charge-transfer nano-complexes hold great potential for further advancing PA imaging in biology and medicine.

Acknowledgements

B. G. X. acknowledges the financial supports from NTU-AIT-MUV NAM/16001, RG110/16 (S), (RG 11/13) and (RG 35/15) awarded in Nanyang Technological University and the National Natural Science Foundation of China (NSFC) (No. 51628201). M. P. thanks the Singapore Ministry of Health's National Medical Research Council (NMRC/OFIRG/0005/2016: M4062012) for financial support. K. Y. P. thanks Nanyang Technological University (Start-Up Grant NTU-SUG: M4081627.120) and Singapore Ministry of Education (Academic Research Fund Tier 1 RG133/15M4011559 and Academic Research Fund Tier 2 MOE2016-T2-1-098) for financial support.

Electronic Supplementary Material: Supplementary material (computational details, SEM, FTIR and XRD measurements, deep tissue photoacoustic signal plot, and diagram of 1,064 nm photoacoustic imaging set up) is available in the online version of this article at <https://doi.org/10.1007/s12274-018-2175-9>.

References

- Wang, L. V.; Hu, S. Photoacoustic tomography: *In vivo* imaging from organelles to organs. *Science* **2012**, *335*, 1458–1462.
- Kim, C.; Favazza, C.; Wang, L. V. *In vivo* photoacoustic tomography of chemicals: High-resolution functional and molecular optical imaging at new depths. *Chem. Rev.* **2010**, *110*, 2756–2782.

- [3] Ntziachristos, V. Going deeper than microscopy: The optical imaging frontier in biology. *Nat. Methods* **2010**, *7*, 603–614.
- [4] Upputuri, P. K.; Pramanik, M. Recent advances toward preclinical and clinical translation of photoacoustic tomography: A review. *J. Biomed. Opt.* **2017**, *22*, 041006.
- [5] Ntziachristos, V.; Razansky, D. Molecular imaging by means of multispectral photoacoustic tomography (MSOT). *Chem. Rev.* **2010**, *110*, 2783–2794.
- [6] Ai, X. Z.; Ho, C. J. H.; Aw, J.; Attia, A. B. E.; Mu, J.; Wang, Y.; Wang, X. Y.; Wang, Y.; Liu, X. G.; Chen, H. B. et al. *In vivo* covalent cross-linking of photon-converted rare-earth nanostructures for tumour localization and theranostics. *Nat. Commun.* **2016**, *7*, 10432.
- [7] Wang, L. V.; Yao, J. J. A practical guide to photoacoustic tomography in the life sciences. *Nat. Methods* **2016**, *13*, 627–638.
- [8] Bozöki, Z.; Pogány, A.; Szabó, G. Photoacoustic instruments for practical applications: Present, potentials, and future challenges. *Appl. Spectrosc. Rev.* **2011**, *46*, 1–37.
- [9] Nie, L. M.; Chen, X. Y. Structural and functional photoacoustic molecular tomography aided by emerging contrast agents. *Chem. Soc. Rev.* **2014**, *43*, 7132–7170.
- [10] Weber, J.; Beard, P. C.; Bohndiek, S. E. Contrast agents for molecular photoacoustic imaging. *Nat. Methods* **2016**, *13*, 639–650.
- [11] Homan, K.; Kim, S.; Chen, Y.-S.; Wang, B.; Mallidi, S.; Emelianov, S. Prospects of molecular photoacoustic imaging at 1064 nm wavelength. *Opt. Lett.* **2010**, *35*, 2663–2665.
- [12] Homan, K. A.; Souza, M.; Truby, R.; Luke, G. P.; Green, C.; Vreeland, E.; Emelianov, S. Silver nanoplate contrast agents for *in vivo* molecular photoacoustic imaging. *ACS Nano* **2012**, *6*, 641–650.
- [13] Ku, G.; Zhou, M.; Song, S. L.; Huang, Q.; Hazle, J.; Li, C. Copper sulfide nanoparticles as a new class of photoacoustic contrast agent for deep tissue imaging at 1064 nm. *ACS Nano* **2012**, *6*, 7489–7496.
- [14] Zhou, Y.; Wang, D. P.; Zhang, Y. M.; Chitgupi, U.; Geng, J. M.; Wang, Y. H.; Zhang, Y. Z.; Cook, T. R.; Xia, J.; Lovell, J. F. A phosphorus phthalocyanine formulation with intense absorbance at 1000 nm for deep optical imaging. *Theranostics* **2016**, *6*, 688–697.
- [15] Jiang, Y. Y.; Upputuri, P. K.; Xie, C.; Lyu, Y.; Zhang, L. L.; Xiong, Q. H.; Pramanik, M.; Pu, K. Y. Broadband absorbing semiconducting polymer nanoparticles for photoacoustic imaging in second near-infrared window. *Nano Lett.* **2017**, *17*, 4964–4969.
- [16] Zhou, J. J.; Jiang, Y. Y.; Hou, S.; Upputuri, P. K.; Wu, D.; Li, J. C.; Wang, P.; Zhen, X.; Pramanik, M.; Pu, K. Y. et al. Compact plasmonic blackbody for cancer theranosis in the near-infrared II window. *ACS Nano* **2018**, *12*, 2643–2651.
- [17] Sun, T. T.; Dou, J.-H.; Liu, S.; Wang, X.; Zheng, X. H.; Wang, Y. P.; Pei, J.; Xie, Z. G. Second near-infrared conjugated polymer nanoparticles for photoacoustic imaging and photothermal therapy. *ACS Appl. Mater. Interfaces* **2018**, *10*, 7919–7926.
- [18] Wu, J. Y. Z.; You, L. Y.; Lan, L.; Lee, H. J.; Chaudhry, S. T.; Li, R.; Cheng, J. X.; Mei, J. G. Semiconducting polymer nanoparticles for centimeters-deep photoacoustic imaging in the second near-infrared window. *Adv. Mater.* **2017**, *29*, 1703403.
- [19] Cheng, K.; Chen, H.; Jenkins, C.; Zhang, Z.; Sun, Z. Y.; Fung, J.; Hong, X. C.; Xing, L.; Cheng, Z. Dual-modal NIR-II fluorescence and photoacoustic imaging of thyroid carcinoma using EGFR-targeted donor-acceptor chromophore based nanoprobe. *J. Nucl. Med.* **2016**, *57*, 556.
- [20] Cheng, K.; Chen, H.; Jenkins, C. H.; Zhang, G. L.; Zhao, W.; Zhang, Z.; Han, F.; Fung, J.; Yang, M.; Jiang, Y. X. et al. Synthesis, characterization, and biomedical applications of a targeted dual-modal near-infrared-II fluorescence and photoacoustic imaging nanoprobe. *ACS Nano* **2017**, *11*, 12276–12291.
- [21] Guo, B.; Sheng, Z. H.; Kenry, H.; Hu, D. H.; Lin, X. W.; Xu, S. D.; Liu, C. B.; Zheng, H. R.; Liu, B. Biocompatible conjugated polymer nanoparticles for highly efficient photoacoustic imaging of orthotopic brain tumors in the second near-infrared window. *Mater. Horiz.* **2017**, *4*, 1151–1156.
- [22] Valluru, K. S.; Willmann, J. K. Clinical photoacoustic imaging of cancer. *Ultrasonography* **2016**, *35*, 267–280.
- [23] Jiang, Y. Y.; Pu, K. Y. Molecular fluorescence and photoacoustic imaging in the second near-infrared optical window using organic contrast agents. *Adv. Biosys.* **2018**, *2*, 1700262.
- [24] Parini, V. P. Organic charge-transfer complexes. *Russ. Chem. Rev.* **1962**, *31*, 408–417.
- [25] Horiuchi, S.; Tokura, Y. Organic ferroelectrics. *Nat. Mater.* **2008**, *7*, 357–366.
- [26] Goetz, K. P.; Vermeulen, D.; Payne, M. E.; Kloc, C.; McNeil, L. E.; Jurchescu, O. D. Charge-transfer complexes: New perspectives on an old class of compounds. *J. Mater. Chem. C* **2014**, *2*, 3065–3076.
- [27] Liu, H. B.; Zhao, Q.; Li, Y. L.; Liu, Y.; Lu, F. S.; Zhuang, J. P.; Wang, S.; Jiang, L.; Zhu, D. B.; Yu, D. P. et al. Field emission properties of large-area nanowires of organic charge-transfer complexes. *J. Am. Chem. Soc.* **2005**, *127*, 1120–1121.
- [28] Liu, Y.; Ji, Z.; Tang, Q.; Jiang, L.; Li, H.; He, M.; Hu, W.; Zhang, D.; Jiang, L.; Wang, X. et al. Particle-size control and patterning of a charge-transfer complex for nanoelectronics. *Adv. Mater.* **2005**, *17*, 2953–2957.
- [29] Qin, Y. K.; Zhang, J.; Zheng, X. Y.; Geng, H.; Zhao, G. Y.; Xu, W.; Hu, W. P.; Shuai, Z. G.; Zhu, D. B. Charge-transfer complex crystal based on extended- π -conjugated acceptor and sulfur-bridged annulene: Charge-transfer interaction and remarkable high ambipolar transport characteristics. *Adv. Mater.* **2014**, *26*, 4093–4099.
- [30] Park, S. K.; Kim, J. H.; Ohto, T.; Yamada, R.; Jones, A. O. F.; Whang, D. R.; Cho, I.; Oh, S.; Hong, S. H.; Kwon, J. E. et al. Highly luminescent 2D-type slab crystals based on a molecular charge-transfer complex as promising organic light-emitting transistor materials. *Adv. Mater.* **2017**, *29*, 1701346.
- [31] Li, Y. J.; Liu, T. F.; Liu, H. B.; Tian, M.-Z.; Li, Y. L. Self-assembly of intramolecular charge-transfer compounds into functional molecular systems. *Acc. Chem. Res.* **2014**, *47*, 1186–1198.
- [32] Grabowski, Z. R.; Rotkiewicz, K.; Rettig, W. Structural changes accompanying intramolecular electron transfer: Focus on twisted intramolecular charge-transfer states and structures. *Chem. Rev.* **2003**, *103*, 3899–4032.
- [33] Nazeeruddin, M. K.; Kay, A.; Rodicio, I.; Humphry-Baker, R.; Müller, E.; Liska, P.; Vlachopoulos, N.; Grätzel, M. Conversion of light to electricity by *cis*-X₂bis(2,2'-bipyridyl-4,4'-dicarboxylate)ruthenium(II) charge-transfer sensitizers (X = Cl⁻, Br⁻, I⁻, CN⁻, and SCN⁻) on nanocrystalline titanium dioxide electrodes. *J. Am. Chem. Soc.* **1993**, *115*, 6382–6390.
- [34] Joseph, P. D.; Eling, T.; Mason, R. P. The horseradish peroxidase-catalyzed oxidation of 3,5,3',5'-tetramethylbenzidine. Free radical and charge-transfer complex intermediates. *J. Biol. Chem.* **1982**, *257*, 3669–3675.
- [35] Bobrow, M. N.; Litt, G. J.; Shaughnessy, K. J.; Mayer, P. C.; Conlon, J. The use of catalyzed reporter deposition as a means of signal amplification in a variety of formats. *J. Immunol. Methods* **1992**, *150*, 145–149.
- [36] Welch, C. L.; Young, D. S. Spectrophotometry of occult blood in feces. *Clin. Chem.* **1983**, *29*, 2022–2025.
- [37] Awano, H.; Ogata, T.; Murakami, H.; Yamashita, T.; Ohigashi, H. Radical salts as charge-transfer complexes between aromatic diamines and their diiminium cations. *Synth. Met.* **1990**, *36*, 263–266.
- [38] Awano, H.; Ohigashi, H. Absorption spectra of the cationic radical salt of 3,3',5,5'-tetramethylbenzidine in acetonitrile. *Bull. Chem. Soc. Jpn.* **1990**, *63*, 2101–2103.
- [39] Vaupel, P.; Kallinowski, F.; Okunieff, P. Blood flow, oxygen and nutrient supply, and metabolic microenvironment of human tumors: A review. *Cancer Res.* **1989**, *49*, 6449–6465.
- [40] Payen, V. L.; Porporato, P. E.; Baselet, B.; Sonveaux, P. Metabolic changes associated with tumor metastasis, part 1: Tumor pH, glycolysis and the pentose phosphate pathway. *Cell. Mol. Life Sci.* **2016**, *73*, 1333–1348.
- [41] Corbet, C.; Feron, O. Tumour acidosis: From the passenger to the driver's seat. *Nat. Rev. Cancer* **2017**, *17*, 577–593.
- [42] McCarty, M. F.; Whitaker, J. Manipulating tumor acidification as a cancer treatment strategy. *Altern. Med. Rev.* **2010**, *15*, 264–272.
- [43] Ivey, J. W.; Bonakdar, M.; Kanitkar, A.; Davalos, R. V.; Verbridge, S. S. Improving cancer therapies by targeting the physical and chemical hallmarks of the tumor microenvironment. *Cancer Lett.* **2016**, *380*, 330–339.
- [44] Kanamala, M.; Wilson, W. R.; Yang, M. M.; Palmer, B. D.; Wu, Z. M. Mechanisms and biomaterials in pH-responsive tumour targeted drug delivery: A review. *Biomaterials* **2016**, *85*, 152–167.
- [45] Holland, V. R.; Saunders, B. C.; Rose, F. L.; Walpole, A. L. A safer substitute for benzidine in the detection of blood. *Tetrahedron* **1974**, *30*, 3299–3302.
- [46] Chung, K.-T.; Chen, S.-C.; Wong, T. Y.; Li, Y.-S.; Wei, C.-I.; Chou, M. W. Mutagenicity studies of benzidine and its analogs: Structure-activity relationships. *Toxicol. Sci.* **2000**, *56*, 351–356.

- [47] Chung, K.-T.; Chen, S.-C.; Claxton, L. D. Review of the salmonella typhimurium mutagenicity of benzidine, benzidine analogues, and benzidine-based dyes. *Mutat. Res./Rev. Mutat. Res.* **2006**, *612*, 58–76.
- [48] Yang, J. H.; Wang, H. S.; Zhang, H. J. One-pot synthesis of silver nanoplates and charge-transfer complex nanofibers. *J. Phys. Chem. C* **2008**, *112*, 13065–13069.
- [49] Gwt, M.; Frisch, H.; Schlegel, G.; Scuseria, M.; Robb, J.; Cheeseman, G.; Scalmani, V.; Barone, B.; Mennucci, G.; Petersson, H., et al. *Gaussian 09*, Revision A. 01; Gaussian Inc.: Wallingford, 2009.
- [50] Emslie, P. H.; Foster, R. Interaction of electron acceptors with bases part 14: Solvent effect on the optical transition of organic charge-transfer complexes. *Recl. Trav. Chim. Pays-Bas* **1965**, *84*, 255–260.
- [51] Wang, C.; Guo, Y. S.; Wang, Y. P.; Xu, H. P.; Wang, R. J.; Zhang, X. Supramolecular amphiphiles based on a water-soluble charge-transfer complex: Fabrication of ultralong nanofibers with tunable straightness. *Angew. Chem., Int. Ed.* **2009**, *48*, 8962–8965.
- [52] Xia, T.; Li, N.; Nel, A. E. Potential health impact of nanoparticles. *Annu. Rev. Public Health* **2009**, *30*, 137–150.
- [53] Sharifi, S.; Behzadi, S.; Laurent, S.; Forrest, M. L.; Stroeve, P.; Mahmoudi, M. Toxicity of nanomaterials. *Chem. Soc. Rev.* **2012**, *41*, 2323–2343.
- [54] Chen, Q.; Liang, C.; Sun, X. Q.; Chen, J. W.; Yang, Z. J.; Zhao, H.; Feng, L. Z.; Liu, Z. H₂O₂-responsive liposomal nanoprobe for photoacoustic inflammation imaging and tumor theranostics via *in vivo* chromogenic assay. *Proc. Natl. Acad. Sci. USA* **2017**, *114*, 5343–5348.